Detection of Hazardous Gas Using Multidemensional Porous Iron Oxide Nanorods-Decorated Carbon Nanoparticles

Dong Hoon Shin, Jun Seop Lee, Jaemoon Jun, Sung Gun Kim, and Jyongsik Jang*

School of Chemical and Biological Engineering, College of Engineering, Seoul National University, 599 Gwanangno, Gwanakgu, Seoul 151-742, Korea

S *Supporting Information*

ABSTRACT: Multidimensional porous iron oxide (Fe_2O_3) nanorods-decorated carbon nanoparticles (MPFCNPs) were fabricated using a dual-nozzle electrospray, thermal stirring, and heat treatment. Polypyrrole (PPy) NPs with FeOOH nanorods were synthesized by electrospraying Fe^{3+} ions, which were adsorbed on the PPy NP surface; the adsorbed Fe^{3+} ions reacted with NaOH to create FeOOH nuclei, and then followed thermal stirring grow nanorods without aggregation. MPFCNPs were fabricated through heat treatment, with the porous structure created in the Fe_2O_3 nanorods by hydroxyl group decomposition. The size of the MPFCNPs and the length of the porous Fe_2O_3 nanorods were controlled by the PPy NP template and concentration of initiator solution, respectively. The MPFCNPs were then utilized as a chemical sensor transducer for NO_2 gas detection at room temperature. The response of the MFPCNP sensor was highly sensitive, displaying a minimum detectable level of 1 ppm; this detection level is lower than that of organic−inorganic hybrid sensors. Moreover, sensitivity also improved with decreasing the diameter of MPFCNPs and increasing Fe_2O_3 nanorod length. The enhanced sensitivity was attributed to the larger surface area presented by the particle size and the porous structure.

KEYWORDS: *multidimensional, Fe_2O_3, electrospray, carbon nanoparticle, NO_2 sensor*
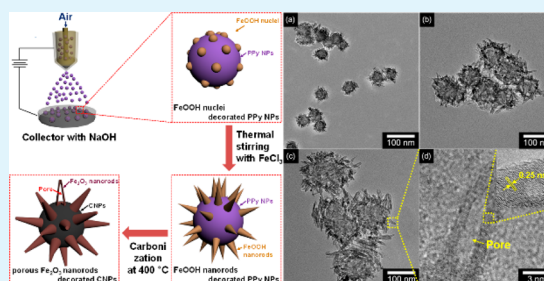
INTRODUCTION

Chemical gas sensors have received much attention in the chemical industry for gas leakage prevention. The most recent research in gas sensors has focused on highly sensitive sensors for the detection of toxic and detrimental gases. Among the harmful gases, nitrogen dioxide (NO_2) not only causes serious damage to the human respiratory system and lung tissue but also induces ozone formation during fossil fuel combustion (e.g., in manufacturing practices, automobiles, and heating systems).[1−4] Therefore, the development of high sensitive sensors is essential for NO_2 detection to minimize environmental exposure.

Over the past several decades, metal oxide nanomaterials, such as ZnO,[5−10] WO_3,[11−14] SnO_2,[15−17] In_2O_3,[18] and Fe_2O_3,[19−22] have been used for gas sensing. Among the metal oxides, iron(III) oxides (Fe_2O_3) are especially promising, due to their attractive chemicophysical properties, including a lower toxicity and high availability. However, metal oxide-based sensors require high operating temperatures, which reduce sensor life and increase power consumption. In many instances, carbon materials have replaced metal oxides in gas-sensing technologies, due to their room temperature operation with better stability. Therefore, much research focuses on carbon materials (carbon nanotubes (CNTs)[23,24] and graphene[25−28]) and conducting polymers (e.g., polypyrrole and polyaniline),[29−31] owing to their high electrical conductivity and chemical inertness, necessary for sensor and electrochromic

devices. However, carbon has a low sensing performance, and conducting polymers have a lower mechanical strength. Therefore, organic-based iron(III) oxide materials may be investigated to resolve the issues presented by its carbon and polymer counterparts.[32−35]

Herein, using a dual-nozzle electrospray, thermal stirring, and heat treatment method, we fabricated carbon nanoparticles whose surfaces were decorated with multidimensional porous iron oxide (Fe_2O_3) nanorods (MPFCNPs). The diameter of the MPFCNPs was controlled by introducing various sizes of polypyrrole (PPy) NPs as the template material. The dual-nozzle electrospray provided FeOOH nanoparticles as nuclei for metal oxide nanorod growth aggregation-free. Thermal treatment in an inert gas created a porous Fe_2O_3 nanorod structure, due to the decomposition of the OH^- group, which provided a high surface area. The MPFCNPs were then utilized as a chemical sensor transducer. The resulting sensing response was highly sensitive and reversible, and resulted in the larger surface area of the multidimensional structure. The minimum detectable level (MDL) was 1 ppm for the MPFCNPs, lower than that for a NO_2 sensor using organic-based metal oxide materials. To our knowledge, this is the first fabrication of

organic-based metal oxide hybrid materials for hazardous gas sensors, using the dual-nozzle electrospray technique.

RESULTS AND DISCUSSION

Fabrication of MPFCNPs. Figure 1 shows the steps in MPFCNP synthesis, which involved the use of a dual-nozzle
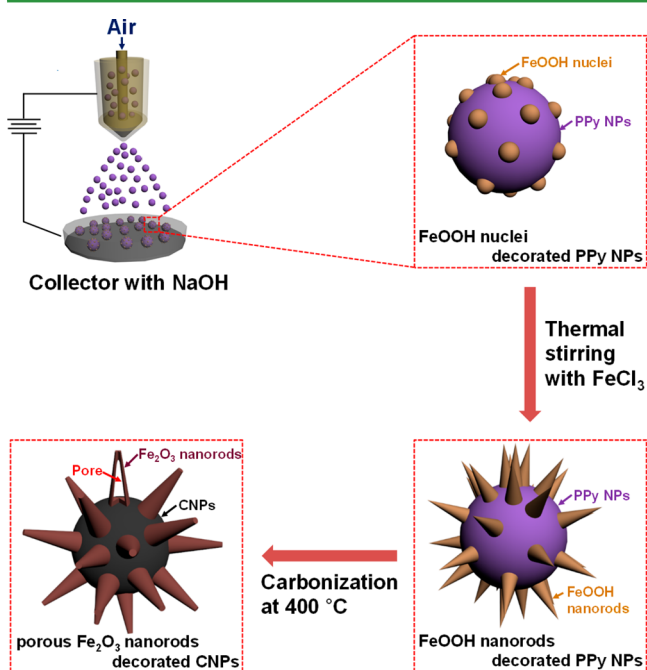

Figure 1. Illustrative diagram of the steps in fabrication of multidimensional porous Fe_2O_3 carbon nanoparticles (MPFCNPs).

electrospray, thermal stirring, and followed by heat treatment. PPy NPs of various sizes (30, 60, and 100 nm) were prepared by adjusting the amount of pyrrole monomer during the chemical oxidation polymerization reaction, as shown in Figure S1 (Supporting Information).[36] The PPy NPs (as the starting material) were then dispersed in an ethanolic $FeCl_3$ solution for adsorbing Fe^{3+} ions on the PPy NP surface before introducing the syringe. The as-prepared mixed solution was electrosprayed through the outlet of the dual-nozzle and compressed air flowed through the nozzle inlet, which resulted in the formation of FeOOH nuclei-decorated PPy NPs. In this system, a high voltage was applied to uniformly disperse the Fe^{3+} ions, and the compressed air minimized particle aggregation. FeOOH nuclei formed as a result of a reaction between Fe^{3+} and NaOH, as shown in Figure S2 (Supporting Information). The FeOOH nuclei-decorated PPy NPs were stirred in $FeCl_3$ solution of various concentrations (1, 5, and 10 wt %) at 70 °C for 4 h, to form FeOOH nanorods.[37−39] Finally, the FeOOH nanorods-decorated PPy NPs were carbonized in an inert gas (Ar) flow to obtain MPFCNPs.

Figure 2a−c shows transmission electron microscopy (TEM) images of the MPFCNPs, having a diameter of 35, 65, and 100 nm, respectively. Thermal treatment was conducted at 300 °C for 2 h to prevent the collapse of the MPFCNPs. As a result of the heat treatment, the FeOOH nanorods were transformed to Fe_2O_3 nanorods with a porous structure (length, ca. 12 nm; pore size, ca. 6 nm), due to the decomposition of the OH^- group of FeOOH.[20,40] Figure 2d shows a high-resolution TEM image and lattice fringe (inset) of the porous Fe_2O_3 nanorods, indicated that FeOOH converted to Fe_2O_3, successfully.
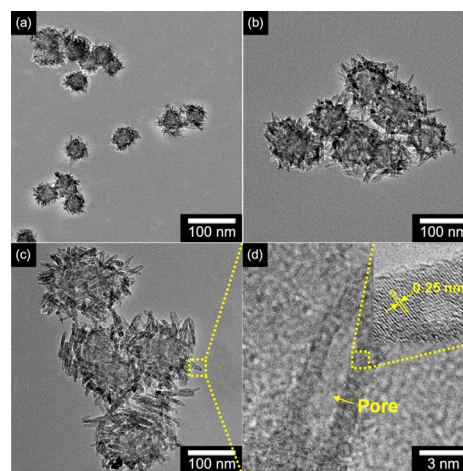

Figure 2. Transmission electron microscopy (TEM) images of MPFCNPs of various sizes: (a) ca. 35, (b) ca. 65, and (c) ca. 100 nm, respectively. (d) High-resolution TEM (HR-TEM) images and lattice fringe (inset) of porous Fe_2O_3 nanorod.

Hereafter, the porous Fe_2O_3 nanorod-decorated carbon nanoparticles, 35, 65, and 100 nm in size, are denoted as MPFCNPs_35, MPFCNPs_65, and MPFCNPs_100, respectively.

Characterization of MPFCNPs. The crystal structures of pristine CNPs and MPFCNPs were investigated by powder X-ray diffraction (XRD) analysis (Figure 3). The broad peak near
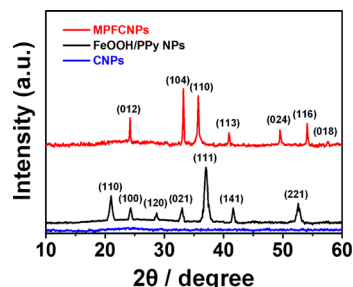

Figure 3. X-ray diffraction (XRD) analysis of CNPs (blue), FeOOH/PPy NPs (black), and MPFCNPs (red).

$2\theta = 23°$ for the CNPs indicated an amorphous carbon phase. The pattern of the MPFCNPs also exhibited a broad peak at about $2\theta = 23°$; the strong peaks for (012), (104), and (110) corresponded to Fe_2O_3. The presence of additional minor peaks, namely, (113), (024), (116), and (018), provided further evidence for the existence of Fe_2O_3 (JCPDS 4-0835). Moreover, XRD spectroscopy of FeOOH nanorods decorated PPy NPs was indicated that not only PPy structure was well maintained during the thermal stirring method but also the sharp peaks were implied the FeOOH phase.

X-ray photoelectron spectroscopy (XPS) was used to determine the chemical composition of the sample for each of the fabrication steps. Figure 4a displays the full spectrum over the range from 0 to 1200 eV. These overview spectra indicated that C, N, and O were present in all of the samples, whereas additional Fe was present in the MPFCNPs by Fe_2O_3 nanorods. A high-resolution XPS spectrum of the C 1s region around 285.5 eV is shown in Figure 4b. The C 1s peak for PPy NPs was ascribed to four peaks positioned at 284.3, 285.3, 286.6, and 284.9 eV, corresponding to C=C, C—C, C—O,
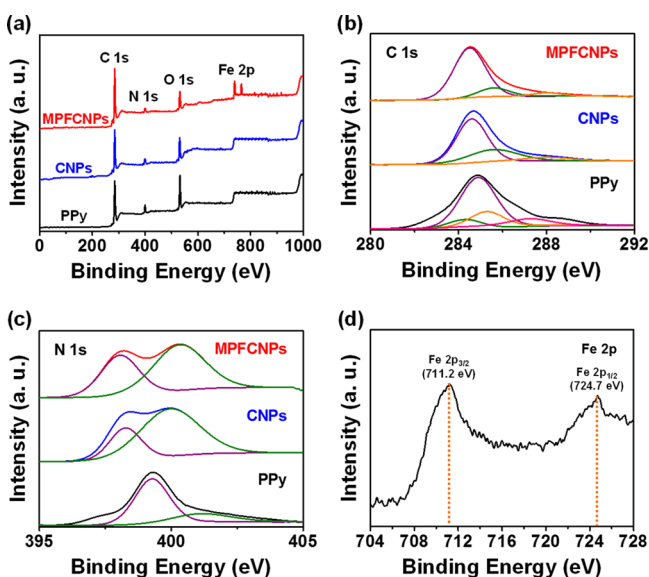
Figure 4. X-ray photoelectron spectroscopy (XPS) of (a) overall scanned spectra and high resolution of (b) C 1s and (c) N 1s of polypyrrole (PPy), CNPs, and MPFCNPs, respectively. (d) Fe 2p of MPFCNPs.

and C—N bonds, respectively. In contrast, the spectra of the CNPs indicated peaks at 284.6 eV for graphitic sp^2, 285.5 eV for C—O bonds, and 287.9 eV for C—N bonds. The C 1s peak for the MPFCNPs was not shifted compared with that for the CNPs, implying that the CNP structure was maintained during porous Fe_2O_3 nanorods formation. Figure 4c shows the N 1s peak for the PPy NPs at 399.4 and 401.3 eV, corresponding to the C—N^+, and C=N^+ bonds. The two peaks, 398.3 and 400 eV, were attributed to pyridinic-N and pyrrolic-N in the CNPs. The N 1s peak of the MPFCNPs showed a similar tendency as that of C 1s, with respect to the CNPs. Spin—orbit components $2p_{3/2}$ and $2p_{1/2}$ (Figure 4d) were measured at 711.2 and 724.7 eV, representing the Fe^{3+} state in the MPFCNPs.

Barrett—Joyner—Halenda (BJH) measurements were performed to identify the pore size distribution of each sample with a diameter of ca. 35 nm (Figure 5). The main peak in the pore size of PPy was 11.5 nm, in good agreement with the characteristic PPy structure, as shown in Figure 5a. After carbonization, the pore size shrank to ca. 7.9 nm, due to the phase change from PPy to amorphous carbon (Figure 5b). Moreover, an additional peak with a diameter of ca. 5 nm was measured for the Fe_2O_3 nanorods (Figure 5c); this feature remained, regardless of the particle diameter (Figure S4, Supporting Information).

Brunauer—Emmett—Teller (BET) measurements were conducted to determine the specific surface area, as shown in Figure S5 (Supporting Information). Given a specific surface area of 62 m^2 g^{-1} for PPy_35, CNPs_35 and MPFCNPs_35 presented values of 95 and 290 m^2 g^{-1}, respectively. The abrupt increase in specific surface area for MPFCNPs_35, compared with the starting material PPy, was attributed to porous Fe_2O_3 nanorod formation. Additionally, our results showed that the smallest sized particles (35 nm) provided the highest surface-to-volume ratio. The specific surface area and pore size distributions are summarized in Table S1 (Supporting Information).

Sensing Performance of the MPFCNPs. The current—voltage (I—V) curves of the MPFCNPs with various sizes are
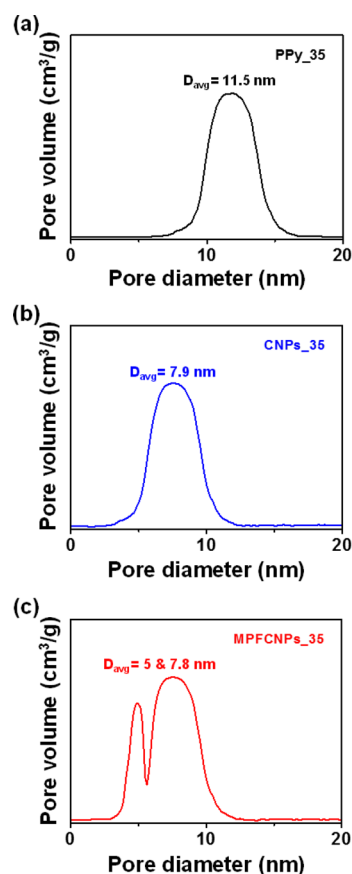

Figure 5. Barrett—Joyner—Halenda (BJH) pore-size distribution curve of (a) PPy, (b) CNPs, and (c) MPFCNPs with a diameter of ca. 35 nm.

shown in Figure 6. All samples exhibited a linear line, implying good electrical contact (Ohmic contact) with the sensor
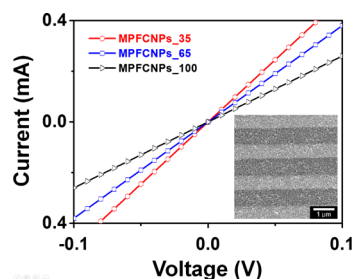

Figure 6. Current—voltage (I—V) curves of various diameter MPFCNPs (35 nm, red; 65 nm, blue; 100 nm, black) deposited on an interdigitated array (IDA) electrode, using the spin-coating method. The inset shows field emission-scanning electron microscopy (FE-SEM) images of the MPFCNPs deposited on the IDA electrode.

substrate. Additionally, field emission-scanning electron microscopy (FE-SEM) images of the MPFCNPs deposited on an interdigitated array (IDA) show that the MPFCNPs were well-aligned, without regions of deficiency or excess (inset of Figure 6).

The Fe_2O_3-based gas sensors with highly sensitive for detecting of NO_2 gas at higher temperatures (ca. 200 °C) were reported in the previous reports.[18−21] In contrast, our MPFCNP sensor exhibited a fast response to NO_2 gas at room
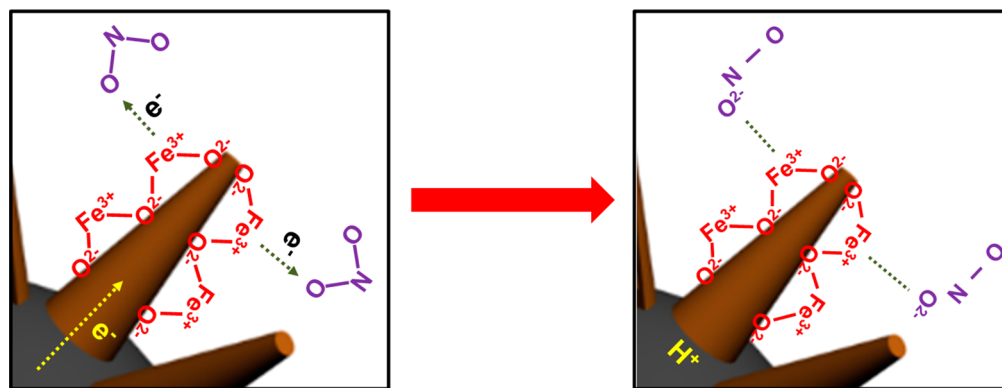
Figure 7. Schematic diagram of the NO$_2$ gas sensing mechanism of MPFCNPs.

temperature via an electron transfer mechanism, as shown in Figure 7.

The sensing mechanism is described as follows. First, the porous Fe$_2$O$_3$ nanorods adsorb the NO$_2$ gas (oxidizing gas), due to its strong electron withdrawing property. The electrons that transfer to the NO$_2$ molecules leave behind electron vacancies in the porous Fe$_2$O$_3$ nanorods. These vacancies are compensated by the electron of CNPs, resulted in increase of holes. Second, porous Fe$_2$O$_3$ (*n*-type) forms a depletion zone with the CNPs (*p*-type), creating a *p*−*n* junction; this allows for more electrons to be transferred from the CNPs to NO$_2$ through Fe$_2$O$_3$.[4,41−43] As a result, the increased number of holes in the CNPs and the depletion zone lead to a decrease in the electrical resistance.

To determine the effect of particle size on sensor response, we measured the sensing test of the NO$_2$ gas with MPFCNPs of various diameters. The real-time response of MPFCNPs was conducted for various concentrations of NO$_2$ gas (Figure 8). When the MPFCNPs were exposed to NO$_2$ gas at room temperature, high sensitivity and rapid response/recovery times were confirmed.

Figure 8a shows the responses upon sequential exposure to NO$_2$ concentrations of 1, 5, 10, 20, and 50 ppm. The resistance decreased with increasing concentration, in agreement with an increase in the number of charge carriers from NO$_2$ electron withdrawing. Furthermore, the sensitivity of MPFCNPs sensors increased with decreasing particle sizes, which indicated that the specific surface area (m^2 g^{-1}: MPFCNPs_35 (310.5) > MPFCNPs_65 (286.8) > MPFCNPs_100 (243.5)) played a major role in the sensing performance. Moreover, the detection limit of the MPFCNPs sensor was considerable lower than previous Fe$_2$O$_3$-based organic NO$_2$ sensors (Table S2, Supporting Information).[32,35]

Figure 8b shows the electrical response of the MPFCNPs upon periodic exposure to 1 ppm of NO$_2$ gas. The change in sensitivity during the cycle test was insignificant, indicating the reversibility of the MPFCNPs sensor for detecting NO$_2$ gas. The MPFCNPs sensors displayed nonlinear sensitivity changes at low concentrations (<1 ppm); the normalized resistance change should be zero at 0 ppm, as shown in Figure 8c. The linear response of the MPFCNPs sensor over the range from 1 to 50 ppm indicated good reversibility and reproducibility to various concentrations, with the response more pronounced with increasing gas concentration.

The influence of the length of the porous Fe$_2$O$_3$ nanorods on sensor sensitivity was examined to determine the influence of Fe$_2$O$_3$, as shown in Figure S6 (Supporting Information). PPy
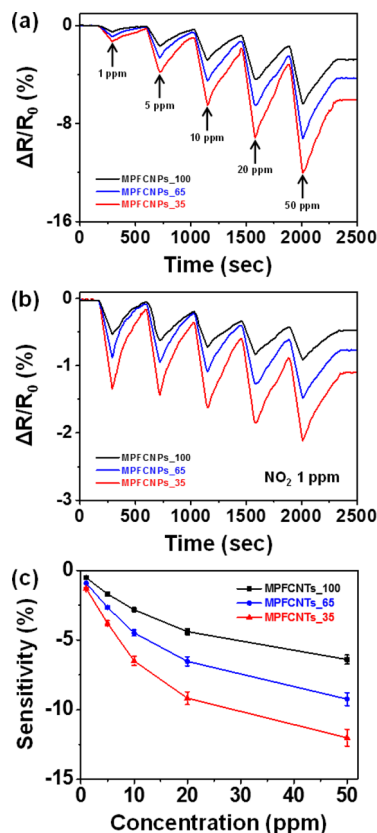

Figure 8. Reversible and reproducible responses were analyzed at a constant current (10^{-6} A) with various sizes of MPFCNPs (35 nm, red; 65 nm, blue; 100 nm, black). Normalized resistance changes upon (a) sequential exposure to different NO$_2$ gas concentrations and (b) periodic exposure to NO$_2$ gas at 1 ppm at room temperature. (c) Calibration line as a function of concentration of NO$_2$ gas.

particles with a diameter of ca. 35 nm were used as the starting materials, due to their high surface areas. The length of the porous Fe$_2$O$_3$ nanorods was controlled by the thermal stirring time; MPFCNPs with long and short porous Fe$_2$O$_3$ nanorods are labeled as MPFCNPs_35_L and MPFCNPs_35_S, respectively.

Figure S6 (Supporting Information) shows the reversible, reproducible response upon sequential exposure, according to various NO$_2$ concentrations. The response of pristine CNPs was very weak. As the length of the porous Fe$_2$O$_3$ nanorods increased, the sensor sensitivity increased; this implies that the Fe$_2$O$_3$ acts as an active site for NO$_2$ gas detection, with longer

nanorod lengths providing additional active sites. Use of the small size CNPs as substrates increased the surface area, which was further enhanced by the porous Fe_2O_3 nanorods, thus enhancing interaction with the NO_2 gas. As a result, the MPFCNPs with 35 nm diameter CNPs (i.e., MPFCNPs_35_L) showed the highest sensitivity, compared with the other samples.

CONCLUSIONS

Multidimensional porous iron oxide (Fe_2O_3) nanorods-decorated carbon nanoparticles (MPFCNPs) were fabricated using dual-nozzle electrospray and thermal stirring, followed by heat treatment. In this procedure, the diameter of the MPFCNPs was controlled by the size of the PPy NPs as the starting material. The change in the structure was induced by the following steps. FeOOH nanorods vertically decorated the surface of the PPy NPs via a dual-nozzle electrospray and thermal stirring technique. The FeOOH nanorods were then converted to Fe_2O_3 nanorods with pores by removal of the hydroxide groups, resulting in a higher surface area. The as-prepared MPFCNPs were utilized for electrodes for NO_2 gas sensing. The MPFCNP sensor demonstrated a high sensitivity at room temperature with decreasing size of the MPFCNPs, because the small size of the MPFCNPs provided a higher specific surface area. As a result, long porous Fe_2O_3 nanorod-decorated 35 nm CNPs exhibited a higher sensitivity, indicating not only a higher surface area but also numerous active sites to interact with NO_2 gas.

EXPERIMENTAL SECTION

Materials. Poly(vinyl alcohol) (PVA, Mw = 9000–10 000, 80% hydrolyzed), a pyrrole (98%) monomer, iron(III) chloride $(FeCl_3)$, and sodium hydroxide (NaOH) were purchased from Aldrich Chemical Co. and used without further purification.

Synthesis of MPFCNPs. PPy nanoparticles of various diameters were prepared with PVA, $FeCl_3$, and pyrrole monomer in deionized water as described in our previous report.[36] Each of the particles was mixed with $FeCl_3$ solution (5 wt %), and then the mixture was stirred for 4 h at room temperature. The mixing solution was injected into a syringe pump (KD Scientific, USA) and pumped into the outer nozzle (20 G nozzle; inner diameter: 0.5 mm) of a dual-nozzle system. Moreover, pressed air flowed through the inner nozzle (27 G nozzle; inner diameter: 0.1 mm). The nozzle was linked to the positive terminal of a power supply to provide a high voltage, i.e., 15 kV, and the resulting dispersed materials were collected in a glass Petri dish containing a NaOH aqueous solution. The flow rate of the syringe pump was fixed at 0.1 mL min^{-1}, and the distance between the nozzle and glass Petri dish was 15 cm. The materials from the electrospray output were dispersed in a various concentration of $FeCl_3$ aqueous solution (1, 5, and 10 wt %) and stirred at 70 °C for 4 h. The resulting solution was washed with ethanol several times, and dried at 60 °C in a vacuum oven. The as-prepared samples were then heated at 5 °C min^{-1} in flowing argon gas to 300 °C, where they were held for 2 h to complete carbonization. PPy NPs were also carbonized for the control experiment.

Characterization of MPFCNPs. Transmission electron microscopy (TEM) and high-resolution TEM (HR-TEM) images were obtained with JEOL JEM-200CX and JEOL JEM-2010F microscopes, respectively. Samples of the nanomaterial were dispersed in ethanol and cast onto copper grids. X-ray photoelectron spectroscopy (XPS) and X-ray diffraction (XRD) spectra were obtained using a JPS-9000MS system (JEOL, X-ray source: Mg $K\alpha$) and M18XHF-SRA (Rigaku, SmartLab, λ = 1.5418 Å) spectrometers, respectively. Brunauer–Emmett–Teller (BET) surface areas and Barrett–Joyner–Halenda (BJH) pore size distributions were measured with an ASAP 2010 analyzer (Micrometrics). Electrical conductivity measure-ments were conducted in ambient atmosphere, using a four-probe technique.

Deposition of MPFCNPs on the IDA. The MPFCNPs were dispersed in ethanol solution using ultrasonication for deposition onto an as-prepared interdigitated array (IDA), using an ultrasonic homogenizer (Autotune 750 W, Cole-Parmer Instruments, Vernon Hills, Illinois, USA). The ultrasonication instrument was operated at a frequency of 15 kHz using a titanium tip with a diameter of 12 mm for 40 min. The samples were deposited on the IDA using a spin-coating method (1000 rpm, 60 s) and dried at room temperature in an inert atmosphere for 1 h to minimize the contact resistance.

Structure and Preparation of the Sensor Device. MPFCNP gas sensors were introduced in a one-side-open cell having a volume of ca. 10 cm^3. Four mass flow controllers (MFCs) were connected to supply single gas flow to the cell. Two MFC lines of synthetic air and NO_2 gas were used to vary the ratio of synthetic air to NO_2 gas. The sensor was exposed to a sequence of VOC pulses for a constant period. The cell was purged with synthetic air between each pulse to enable sensor recovery.

Electrical Measurement of Sensitivities in MPFCNPs Sensor. The resistance change in the MPFCNPs was monitored and recorded with a source meter connected to a computer. The MPFCNPs sensors were placed in a vacuum chamber with a vapor inlet/outlet (ca. 100 Torr). Various NO_2 gas concentrations (1–50 ppm) were injected into the chamber by the MFC. The real-time resistance value (defined as $\Delta R/R_0 = (R - R_0)/R_0$, where R and R_0 are the real-time and initial resistance, respectively) was recorded for a constant applied current of 10^{-6} A. After the MPFCNP sensor was exposed to several cycles of NO_2 gas, the gas vapor was replaced with pressed air to remove the attached NO_2 molecules from the nanomaterial.

ASSOCIATED CONTENT

Ⓢ Supporting Information

(1) TEM images of PPy NPs with various sizes; (2) formation mechanism of FeOOH nuclei; (3) BJH curve of PPy, CNPs and MPFCNPs with various diameters; (4) BET curve of PPy, CNPs and MPFCNPs with various diameters; (5) surface area and main pore size of each samples; (6) sensing performance of MPFCNPs compared to other Fe_2O_3-based organic materials report; (7) TEM images of CNPs, MPFCNPs with short and long nanorod; (8) sensing performance of CNPs, MPFCNPs with short and long nanorods. This material is available free of charge via the Internet at http://pubs.acs.org.

AUTHOR INFORMATION

Corresponding Author
*J. Jang. Tel: +82-2-880-7069. Fax: +82-2-888-1604. E-mail: jsjang@plaza.snu.ac.kr.

Notes
The authors declare no competing financial interest.

ACKNOWLEDGMENTS

REFERENCES

(1) Kreuzer, L. B.; Patel, C. K. N. Nitric Oxide Air Pollution: Detection by Optoacoustic Spectroscopy. *Science* **1971**, *173*, 45–47.

(2) Han, N. R.; Ye, J. S.; Yu, A. C.; Sheu, F. Differential Mechanisms Underlying the Modulation of Delayed-Rectifier K^+ Channel in Mouse Neocortical Neurons by Nitric Oxide. *J. Neurophysiol.* **2006**, *95*, 2167–2178.

(3) Andringa, A.-M.; Piliego, C.; Katsouras, I.; Blom, P. M.; Leeuw, D. M. NO_2 Detection and Real-Time Sensing with Field-Effect Transistors. *ACS Appl. Mater. Interfaces* **2014**, *26*, 773–785.

(4) Delen, F. M.; Sippel, J. M.; Osborne, M. L.; Law, A.; Thukkani, N.; Holden, W. E. Increased Exhaled Nitric Oxide in Chronic Bronchitis: Comparison with Asthma and COPD. *Chest* **2000**, *117*, 695−701.

(5) Park, S.; An, S.; Ko, H.; Jin, C.; Lee, C. Synthesis of Nanograined ZnO Nanowires and Their Enhanced Gas Sensing Properties. *ACS Appl. Mater. Interfaces* **2012**, *4*, 3650−3656.

(6) Andringa, A.; Meijboom, J. R.; Smits, E. C. P.; Mathijssen, S. G. J.; Blom, P. W. M.; Leeuw, D. M. Gate-Bias Controlled Charge Trapping as a Mechanism for NO_2 Detection with Field-Effect Transistors. *Adv. Funct. Mater.* **2011**, *21*, 100−107.

(7) Rai, P.; Kwak, W.-K.; Yu, Y.-T. Solvothermal Synthesis of ZnO Nanostructures and Their Morphology-Dependent Gas-Sensing Properties. *ACS Appl. Mater. Interfaces* **2013**, *5*, 3026−3032.

(8) Shouli, B.; Liangyuan, C.; Dingqing, L.; Wensheng, Y.; Pengcheng, Y.; Zhiyong, L.; Aifan, C.; Liu, C. C. Different Morphologies of ZnO Nanorods and Their Sensing Property. *Sens. Actuators, B* **2010**, *146*, 129−137.

(9) Pan, X.; Liu, X.; Bermak, A.; Fan, Z. Self-Gating Effect Induced Large Performance Improvement of ZnO Nanocomb Gas Sensors. *ACS Nano* **2013**, *7*, 9318−9324.

(10) Andringa, A.-M.; Piliego, C.; Katsouras, I.; Blom, P. M.; Leeuw, D. M. NO_2 Detection and Real-Time Sensing with Field-Effect Transistors. *Chem. Mater.* **2014**, *26*, 773−785.

(11) Van, P. T. H.; Thanh, N. H.; Quang, V. V.; Duy, N. V.; Hoa, N. D.; Hieu, N. V. Scalable Fabrication of High-Performance NO_2 Gas Sensors Based on Tungsten Oxide Nanowires by On-Chip Growth and RuO_2-Functionalization. *ACS Appl. Mater. Interfaces* **2014**, *6*, 12022−12030.

(12) Srivastava, S.; Jain, K.; Shingh, V. N.; Singh, S.; Vijayan, N.; Dilawar, N.; Gupta, G.; Senguttuyan, T. D. Faster Response of NO_2 Sensing in Graphene−WO_3 Nanocomposites. *Nanotechnology* **2012**, *23*, 205501−205507.

(13) Zeng, J.; Hu, M.; Wang, W.; Chen, H.; Qin, Y. NO_2-Sensing Properties of Porous WO_3 Gas Sensor Based on Anodized Sputtered Tungsten Thin Film. *Sens. Actuators, B* **2012**, *161*, 447−452.

(14) Bai, S.; Zhang, K.; Luo, R.; Li, D.; Chen, A.; Liu, C. C. Low-Temperature Hydrothermal Synthesis of WO_3 Nanorods and Their Sensing Properties for NO_2. *J. Mater. Chem.* **2012**, *22*, 12643−12650.

(15) Kaur, J.; Roy, S. C.; Bhatnagar, M. C. Highly Sensitive SnO_2 Thin Film NO_2 Gas Sensor Operating at Low Temperature. *Sens. Actuators, B* **2007**, *123*, 1090.

(16) Maiti, A.; Rodriguez, J. A.; Law, M.; Kung, P.; McKinney, J. R.; Yang, P. SnO_2 Nanoribbons as NO_2 Sensors: Insights from First Principles Calculations. *Nano Lett.* **2003**, *3*, 1025−1028.

(17) Choi, S. W.; Katoch, A.; Sun, G.; Wu, P.; Kim, S. S. NO_2-Sensing Performance of SnO_2 Microrods by Functionalization of Ag Nanoparticles. *J. Mater. Chem. C* **2013**, *1*, 2834−2841.

(18) Zhang, D.; Liu, Z.; Li, C.; Tang, T.; Liu, X.; Han, S.; Lei, B.; Zhou, C. Detection of NO_2 down to ppb Levels Using Individual and Multiple In_2O_3 Nanowire Devices. *Nano Lett.* **2004**, *4*, 1919−1924.

(19) Neri, G.; Bonavita, A.; Galvagno, S.; Siciliano, P.; Capone, S. CO and NO_2 Sensing Properties of Doped-Fe_2O_3 Thin Films prepared by LPD. *Sens. Actuators, B* **2002**, *82*, 40−47.

(20) Wang, Y.; Wang, S.; Zhang, H.; Gao, X.; Yang, J.; Wang, L. Brookite TiO_2 decorated α-Fe_2O_3 Nanoheterostructures with Rod Morphologies for Gas Sensor Application. *J. Mater. Chem. A* **2014**, *2*, 7935−7943.

(21) Chen, J.; Xu, L.; Li, W.; Gou, X. α-Fe_2O_3 Nanotubes in Gas Sensor and Lithium-Ion Battery Applications. *Adv. Mater.* **2005**, *17*, 582−586.

(22) Nalage, S. R.; Navale, S. T.; Chougule, M. A.; Pawar, S. G.; Sen, S.; Patil, V. B. Development of Fe_2O_3 Sensor for NO_2 Detection. *AIP Conf. Proc.* **2013**, *1512*, 504−505.

(23) Mittal, M.; Kumar, A. Carbon Nanotube (CNT) Gas Sensors for Emissions from Fossil Fuel Burning. *Sens. Actuators, B* **2014**, *203*, 349−362.

(24) Zanolli, Z.; Leghrib, R.; Felten, A.; Pireaux, J.; Liobet, E.; Charlier, J. Gas Sensing with Au-Decorated Carbon Nanotubes. *ACS Nano* **2011**, *2*, 4592−4599.

(25) Schedin, F.; Grim, A. K.; Morozov, S. V.; Hill, E. W.; Blake, P.; Katsnelson, M. I.; Novoselov, K. S. Detection of Individual Gas Molecules Adsorbed on Graphene. *Nat. Mater.* **2007**, *6*, 652−655.

(26) Fowler, J. D.; Allen, M. J.; Tung, V. C.; Yang, Y.; Kaner, R. B.; Weiller, B. H. Practical Chemical Sensors from Chemically Derived Graphene. *ACS Nano* **2009**, *3*, 301−306.

(27) Dua, V.; Surwade, S. P.; Annu, S.; Agnihotra, S. R.; Jain, S.; Roberts, K. E.; Park, S.; Ruoff, R. S.; Manohar, S. K. All-Organic Vapor Sensor Using Inkjet-Printed Reduced Graphene Oxide. *Angew. Chem., Int. Ed.* **2010**, *49*, 2154−2157.

(28) Han, T. H.; Huang, Y.; Tan, A. T. L.; Dravid, V. P.; Huang, J. Steam Etched Porous Graphene Oxide Network for Chemical Sensing. *J. Am. Chem. Soc.* **2011**, *133*, 15264−45267.

(29) Huang, L.; Wang, Z.; Zhang, J.; Pu, J.; Lin, Y.; Xu, S.; Shen, L.; Chen, Q.; Shi, W. Fully Printed, Rapid-Response Sensors Based on Chemically Modified Graphene for Detecting NO_2 at Room Temperature. *ACS Appl. Mater. Interfaces* **2014**, *6*, 7426−7433.

(30) Haynes, A. S.; Gouma, P. I. Electrospun Conducting Polymer-based Sensors for Advanced Pathogen Detection. *IEEE Sens. J.* **2008**, *8*, 701−708.

(31) Ram, M. K.; Yavuz, O.; Aldissi, M. NO_2 Gas Sensing Based on Ordered Ultrathin Films of Conducting Polymer and Its Nano-composite. *Synth. Met.* **2005**, *151*, 77−84.

(32) Navale, S. T.; Khuspe, G. D.; Chougule, M. A.; Patil, V. B. Camphor Sulfonic Acid Doped PPy/α-Fe_2O_3 Hybrid Nanocomposites as NO_2 Sensors. *RSC Adv.* **2014**, *4*, 27998−28004.

(33) Radhakrishnan, S.; Krishnamoorthy, K.; Sekar, C.; Wilson, J.; Kim, S. J. A Highly Sensitive Electrochemical Sensor for Nitrite Detection Based on Fe_2O_3 Nanoparticles Decorated Reduced Graphene Oxide Nanosheets. *Appl. Catal., B* **2014**, *148−149*, 22−28.

(34) Navale, S. T.; Khuspe, G. D.; Chougule, M. A.; Patil, V. B. Polypyrrole, α-Fe_2O_3 and Their Hybrid Nanocomposite Sensor: An Impedance Spectroscopy Study. *Org. Electron.* **2014**, *15*, 2159−2167.

(35) Navale, S. T.; Khuspe, G. D.; Chougule, M. A.; Patil, V. B. Room Temperature NO_2 Gas Sensor based on PPy/α-Fe_2O_3 Hybrid Nanocomposites. *Ceram. Int.* **2014**, *40*, 8013−8020.

(36) Hong, J. Y.; Jang, J. A Comparative Study on Electrorheological Properties of Various Silica−Conducting Polymer Core−Shell Nano-spheres. *Soft Matter* **2010**, *6*, 4669−4671.

(37) Lee, J. S.; Shin, D. H.; Jun, J.; Jang, J. Multidimensional Polypyrrole/Iron Oxyhydroxide Hybrid Nanoparticles for Chemical Nerve Gas Agent Sensing Application. *ACS Nano* **2013**, *7*, 10139−10147.

(38) Lee, J. S.; Jun, J.; Shin, D. H.; Jang, J. Urchin-like Polypyrrole Nanoparticles for Highly Sensitive and Selective Chemiresistive Sensor Application. *Nanoscale* **2014**, *6*, 4188−4194.

(39) Lee, J. S.; Shin, D. H.; Jun, J.; Lee, C.; Jang, J. Fe_3O_4/Carbon Hybrid Nanoparticle Electrodes for High-Capacity Electrochemical Capacitors. *ChemSusChem* **2014**, *7*, 1676−1683.

(40) Wang, J.; Li, L.; Wong, C. L.; Sun, L.; Shen, Z.; Madhavi, S. Controlled Synthesis of α-FeOOH Nanorods and Their Trans-formation to Mesoporous α-Fe_2O_3, Fe_3O_4@C Nanorods as Anodes for Lithium Ion Batteries. *RSC Adv.* **2013**, *3*, 15316−15326.

(41) Maeng, S.; Kim, S. W.; Lee, D. H.; Moon, S. E.; Kim, K. C.; Maiti, A. SnO_2 Nanoslab as NO_2 Sensor: Identification of the NO_2 Sensing Mechanism on a SnO_2 Surface. *ACS Appl. Mater. Interfaces* **2014**, *6*, 357−363.

(42) Pokhrel, S.; Simon, C. E.; Teodorescu, V. S.; Barsan, N.; Weimar, U. Synthesis, Mechanism, and Gas-Sensing Application of Surfactant Tailored Tungsten Oxide Nanostructures. *Adv. Funct. Mater.* **2009**, *19*, 1767−1774.

(43) Ivanovskaya, M.; Kotsikau, D.; Faglia, G.; Nelli, P.; Irkaev, S. Gas-Sensitive Properties of Thin Film Heterojunction Structures based on Fe_2O_3−In_2O_3 Nanocomposites. *Sens. Actuators, B* **2003**, *7031*, 1−9.